Rare Metal Materials and Engineering
Volume 53, Issue 3, March 2024
Available online at www.rmme.ac.cn

Science Press

Cite this article as: Wang Qiuping, Guan Jieren. Microstructure Characteristic and Its Impact on Nano-hardness of LPBF-Processed Al-based Alloy with Ti Addition[J]. Rare Metal Materials and Engineering, 2024, 53(03): 676-684. DOI: 10.12442/j.issn.1002-185X.20230371.

ARTICLE

Microstructure Characteristic and Its Impact on Nano-hardness of LPBF-Processed Al-based Alloy with Ti Addition

Wang Qiuping, Guan Jieren

Marine Equipment and Technology Institute, Jiangsu University of Science and Technology, Zhenjiang 212003, China

Abstract: The influence of Ti addition into Al-based alloy fabricated by laser powder bed fusion (LPBF) technique was demonstrated. The microstructure characteristics, phase identification and nano-hardness of the LPBF-processed samples without or with 3wt% Ti addition were investigated by scanning electron microscope, electron backscatter diffraction, X-ray diffraction, transmission electron microscope and nano-indentation tests. The results reveal that a refined grain microstructure and lower average grain sizes can be obtained. Due to the heterogeneous nucleation provided by Al_3Ti precipitated phases, the ranges of grain sizes are reduced within 2.5 μm. As the low angle grain boundary increases, higher crystal lattice distortion energy contributes to the increase in average nano-hardness (to 2.36 GPa) and Young's modulus (to 92.72 GPa) values. The <100> texture of LPBF-processed Al-based alloy with 3wt% Ti addition is slightly enhanced, while there is still a random crystal orientation. The phase transformation from α-Al to Al_3Ti can be obtained.

Key words: laser powder bed fusion; microstructure; precipitated phase; nano-hardness; grain size

Laser powder bed fusion (LPBF) is a laser-based and powder-based additive manufacturing technology that fabricates three dimensional components in a track-by-track and layer-by-layer fashion[1–2]. Complex structures and geometries can be conventionally produced with a high relative density up to 99.9% by LPBF for metallic alloys and composites[3–4]. Attributed to the characteristics of high cooling rates and rapid solidification, columnar and equiaxed grains were frequently observed[5–6]. The columnar grains are characterized by anisotropic mechanical properties, while the equiaxed grains are more uniform[7]. Due to the advantages of recyclable powders and design freedom, the LPBF technique has been extensively developed and applied in aerospace, automotive industry and biomedical fields[8–9]. Till now, nickel-based superalloy[10–12], copper alloys[13–15] and titanium alloys[16–18] have become the main focus for industrial applications, which are reported recently, detailing the existing state-of-the-art corresponding to LPBF processing.

With the increasing demand for lightweight and thermal conductivity in the automotive industry, aluminium-silicon (Al-Si) alloys have received great interests in relevant researches[19–20]. Because of the reason for near-eutectic composition in Al-Si alloys, the characteristics of good weldability and fluidity can greatly reduce cracking risks in LPBF process[21]. Due to the precipitation of Mg_2Si particles as a hardening phase upon aging treatments, the Al-Si alloy with a small amount of Mg is widely used in casting alloys[22]. Previous studies on the LPBF-processed AlSi10Mg alloys involved processing parameters optimization and heat treatment to achieve better mechanical properties, such as fatigue and tensile properties[23–26]. In recent years, aluminium alloys reinforced with ceramic particles (aluminium matrix composites) have attracted great attention for superior performance utilizing mixture and "in-situ" reactions[27]. Wang et al[28] added nano-metric TiC powders into AlSi10Mg alloys to prepare nano-composites by high-energy ball milling. The hardness and tensile strengths of LPBF-processed samples are much higher than those of unreinforced parts. Yuan et al[29] adopted a simulation method to explore the temperature distribution and thermal behaviour of the molten pool in TiC/

Received date: June 12, 2023
Foundation item: Natural Science Foundation for Colleges and Universities of Jiangsu Province (22KJB430023); Youth Science and Technology Innovation Project of Jiangsu University of Science and Technology (1172922101)
Corresponding author: Guan Jieren, Ph. D., Marine Equipment and Technology Institute, Jiangsu University of Science and Technology, Zhenjiang 212003, P. R. China, E-mail: guanjrkmust@163.com

Copyright © 2024, Northwest Institute for Nonferrous Metal Research. Published by Science Press. All rights reserved.

AlSi10Mg composites during LPBF process. The simulation results provide guidance for applying appropriate processing parameters to avoid pores and cracks in practical experiments. Zhao et al[30] used the slurry ball milling process to prepare carbon nanotubes/AlSi10Mg composites, and observed carbon dispersion strengthening and reduced electrical resistivity in LPBF-processed samples. Li et al[31] introduced powder metallurgy technology to in-situ synthesize nano-TiB_2 reinforced AlSi10Mg composites powders, which are suitable for LPBF process. Non-equilibrium solidification characteristics exhibit a coherent interface between nano-TiB_2 particles and Al substrate, resulting in excellent ductility and high tensile strength. Zhao et al[32] synthetized SiC ceramic reinforced Al-based composites by LPBF. The nano-hardness and elastic modulus can be achieved to 2.27 and 78.94 GPa, respectively, because of the in-situ formation of Al_4SiC_4 phases in the molten pool. Due to the heterogeneous nucleation effect provided by the in-situ formed Al_3Zr particles, the crack-free and equiaxed microstructure results in high strengths during LPBF process by coating 1vol% hydrogen-stabilized zirconium on the surface of 7XXX and 6XXX aluminium alloys through electrostatic assembly technique[33]. As a homologous element with Zr, small addition of titanium (Ti) can also exert similar effects to refine the solidification structure of aluminium[34]. In conventional casting of aluminium alloy, incorporation with Ti is a common method to promote grain refinement. Zhang et al[35] adopted thermodynamic calculations to determine the range (0wt%–2wt%) of Ti modified Al-Cu-Mg alloys. Utilizing the gas-atomized powders with Ti content within 1.5wt% during LPBF process, the heterogeneous nucleation provided by Al_3Ti precipitates can effectively promote the grain refinement and eliminate hot tearing cracks. However, the microstructure characteristics and its formation mechanism with external Ti addition have not been reported so far.

This research aims to prepare Al-based alloy/Ti mixed powders by low-energy ball milling. The microstructure characteristics, phase identification and formation mechanism of composites produced by LPBF were analyzed by means of advanced characterization techniques. The influence of LPBF-processed samples without or with Ti addition on the grain boundary distribution and measured nano-hardness was also discussed.

1 Experiment

1.1 Materials and mixing

The feedstock AlSi10Mg alloy was gas atomized powders with particle size of 15–53 μm. To increase the powder bed density, smaller sizes of Ti powders were adopted. The distribution of gas atomized micron Ti particle (TA0) diameters was D_{10}=6.64 μm, D_{50}=12.9 μm and D_{90}=23.4 μm. The determined chemical composition of AlSi10Mg powders was 9.41wt% Si, 0.42wt% Mg and the balance Al. The morphology of two types of powders was recorded by SEM (TESCAN VEGA3, Czech Republic). Most powders show a regular spherical morphology, as shown in Fig.1a and 1b.

According to the Zhang's calculation results, the refinement of predicted grain size is limited when the Ti content is over 1.5wt%[33]. To verify the conclusion, a double content of Ti was introduced. Mixed powders with 3wt% Ti were prepared using a low energy ball milling with a rotation rate of 300 r/min and a holding time of 30 min. The mixture powders were heated in an oven with a temperature of 80 °C to reduce the humidity and moisture of the powder surface for flowability characterization. Fig. 2 shows the distribution and morphology of AlSi10Mg/Ti mixed powders with 3wt% Ti. Most powders display a nearly spherical shape, and no agglomeration phenomenon can be observed. Fig. 2a–2b are SEM image (left) and back-scattered electron image (right) with the same Ti content, respectively, in which the grey particles differ from white particles in element identification. Due to the trace Ti added into AlSi10Mg powders, the distribution of Ti particles is random. Through energy dispersive spectroscope (EDS) point scanning as indicated in Fig. 2c, the Ti element can be found at point 2, and the Al and Si elements can be detected at point 1.

1.2 Processing parameters and equipment

The LPBF experiments were performed on a self-developed machine (Yongnian, Jiangsu, China), as shown in Fig. 3. The equipment was equipped with a 200 W Nd: YAG fibre laser operated at 1060 nm. The laser spot diameter was set at approximately 80 μm. After a series of trial runs, a zigzag

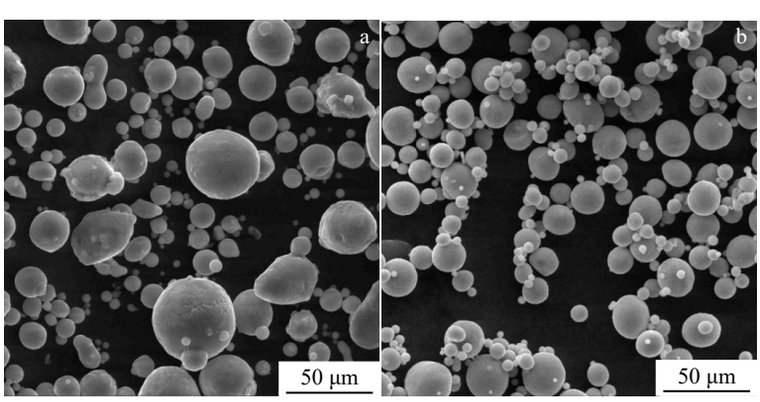

Fig.1 Morphologies of powder particles: (a) AlSi10Mg and (b) Ti

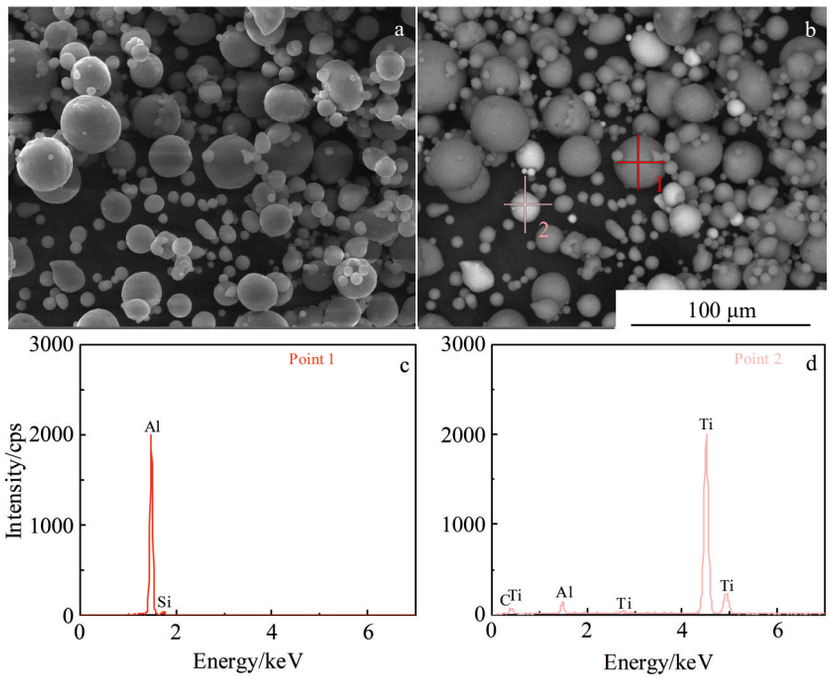

Fig.2 Distribution and morphology of AlSi10Mg/Ti mixed powders (a–b) and corresponding EDS spectra (c–d)

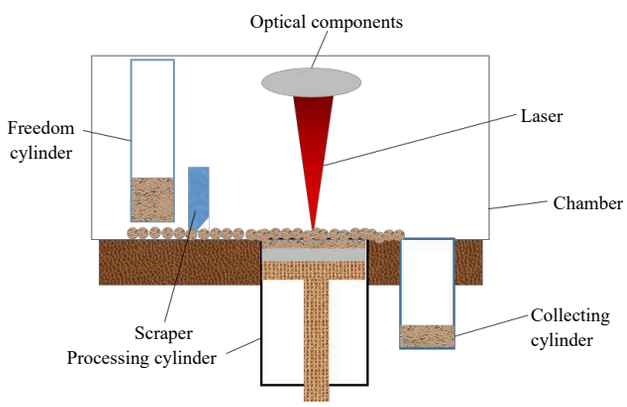

Fig.3 Schematic of LPBF

scanning strategy was applied to achieve AlSi10Mg/Ti samples with the optimized processing parameters as: laser power (P) =200 W, scanning speed (v) =1100 mm/s, hatch space (h)=70 μm and layer thickness (t)=20 μm. As a control group, a LPBF-processed AlSi10Mg without Ti addition was also prepared. The closed processing chamber was pumped to high vacuum conditions and then filled with argon atmosphere to control the oxygen level below 100 μL/L. To compensate heat dissipation and to reduce residual stress, the heating temperature under the substrate was set at 100 °C. During LPBF, the mixed powders were spread homogeneously on the substrate by scraper and laser beam scanned pre-spread powders selectively. Finally, the samples with dimensions of 10 mm×10 mm×5 mm were fabricated accordingly.

1.3 Material characterization techniques

After being removed from the substrate through electrical discharge machining, the samples were placed in ethanol and cleaned by ultrasound wave at room temperature for 30 min. The specimens were then polished, ground and etched with 0.5vol% HNO_3 for 5 s. SEM (ZEISS EVO 18, Germany) and X-ray diffractometer (XRD, MiniFlex600, Japan) with Cu-Kα radiation were utilized for the identification of microstructure morphology and phases, respectively. A transmission electron microscope (TEM, TECNAI G2, Holland) equipped with EDS analysis was used to investigate the element distribution and crystal structures of phases. The LPBF-processed samples with thickness of 100 nm were prepared by the ion-milling technique. The electron backscatter diffraction (EBSD) was conducted on a Hitachi S-3400N SEM equipped with a HKL-EBSD system to investigate the grain sizes and texture intensity. An array of 25×25 indentations with a square area of 145 μm×145 μm on the microstructure was implemented with an iNano instrument (Nanomechanics, Inc., America) to evaluate the nano-hardness and Young's modulus values with or without 3wt% Ti addition. Before the nano-indentation tests, the surface of the sample was polished according to the standard procedures. Indentations were performed at room temperature to a peak force of 5 mN at a rate of approximately one indent per second.

2 Results and Discussion

2.1 Microstructure morphology and phase identification

Fig. 4a reveals a very fine cellular-dendritic solidification structure in LPBF-processed AlSi10Mg sample without Ti addition. Higher cooling rates hinder the fern-like structure growth, resulting in the formation of cell-like substructure (it should be noted that the terminology throughout the paper,

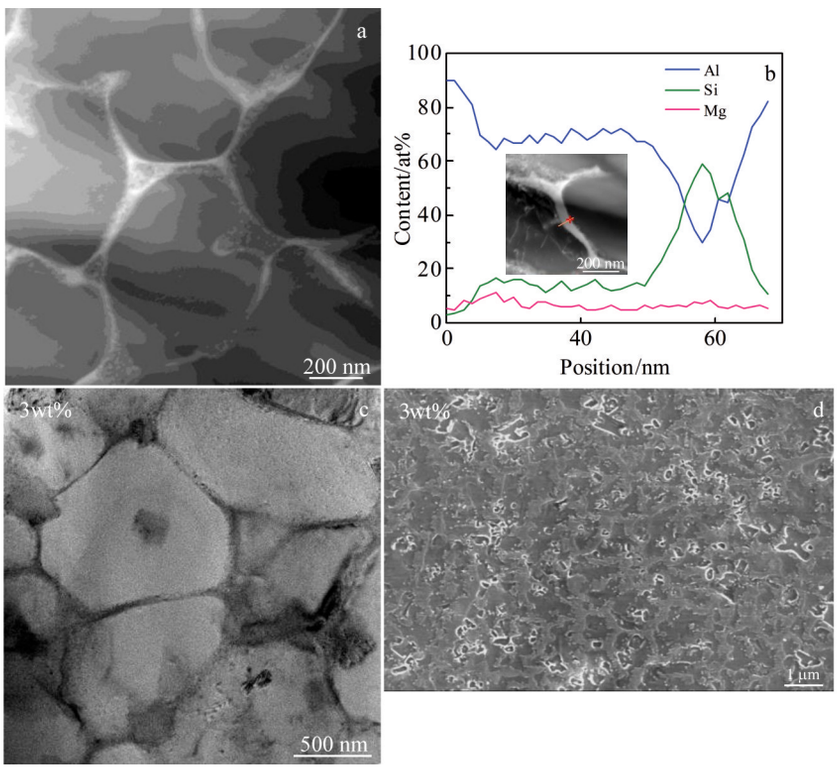

Fig.4 TEM image of Al-Si eutectic microstructure (a); line mapping results along the cell boundary (b); TEM image of new phases distribution (c); SEM image of microstructure morphology with 3wt% Ti addition (d)

e.g. cell, is used to describe different microstructures[36]). The cell boundaries are visible and characterized with the line scanning results in Fig. 4b. The grey cellular features are primary Al and decorated with white net-connected Si particles (Al-Si eutectic) [37]. The element distribution image indicates the presence of Mg element, which should be in the form of Mg_2Si phase[38]. However, only a face-centred cubic α-Al and Si phase can be detected from XRD patterns in Fig. 5. This may be attributed to the lower contents of Mg element. After adding 3wt% Ti particles into Al-based alloy, the microstructure shows different morphologies. From the microscopic scale in Fig. 4c, some new phases appear inside grains or are situated at cell boundary. On mesoscopic scale, some substances precipitate from the matrix, as shown in Fig. 4d. These can be further explained in Section 2.3.

XRD patterns of LPBF-processed AlSi10Mg samples without Ti addition (blue curve) and AlSi10Mg/Ti composites (pink curve) obtained within a wide 2θ range ($20°-90°$) are shown in Fig. 5. Through further examination of the XRD patterns, strong diffraction peaks corresponding to α-Al are identified, mainly existing along five crystal planes of (111), (200), (220), (311) and (222). The peak intensity of Si along the crystal planes of (111) and (110) is relatively lower than that of Al because of low mass percentage. This is consistent with the results of microstructure observation. The 2θ locations of the Al diffraction peaks of LPBF-processed AlSi10Mg/Ti composites

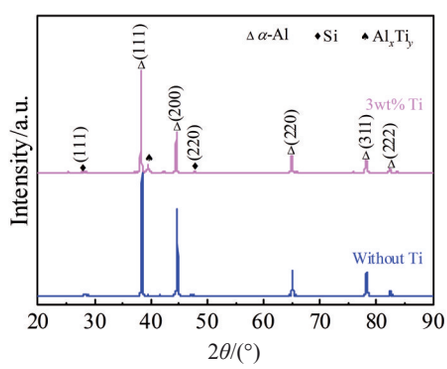

Fig.5 XRD patterns of LPBF-processed samples without and with 3wt% Ti addition

shift to lower 2θ when the Ti proportion is 3wt%. This can be attributed to the changes of cell parameters. The atomic radius of Al (143 pm) is slightly smaller than that of Ti (147 pm) [39]. When the Ti atom sinks into the Al crystal lattice, the cell parameters change. Combined with the Bragg law, the increase in crystal plane spacing results in the decrease in 2θ.

To verify the occurrence of crystalline dimension, Table 1 lists the values of diffraction angle (2θ) and full width at half maximum (FWHM). According to Scherrer formula, the mean crystallite size (D) can be determined using the following expression[40]:

Table 1 Diffraction angle (2θ) and FWHM of Al diffraction peaks

Crystal plane		(111)	(200)	(220)	(311)	(222)
Without Ti	2θ/(°)	38.441	44.681	65.101	78.241	82.462
	θ/(°)	19.221	22.341	32.551	39.121	41.231
	FWHM	0.137	0.162	0.206	0.262	0.271
3wt% Ti	2θ/(°)	38.261	44.521	64.941	78.122	82.361
	θ/(°)	19.131	22.2605	32.471	39.061	41.181
	FWHM	0.165	0.199	0.260	0.344	0.326

$$D = \frac{k\lambda}{\beta \cos\theta} \tag{1}$$

Herein, k is constant (0.89), λ is radiation wavelength (0.154 186 nm), β is the FWHM and θ is the diffraction angle. According to Eq.(1), the crystallite sizes decrease after adding 3wt% Ti powders, but the FWHM appears to be large. This can satisfy the relationship between D and FWHM. The intensity of Al diffraction peaks decreases along all crystal plane. At the vicinity of (111) crystal plane, Al_xTi_y compounds (Al-Ti intermetallic phases) can precipitate from the Al substrate. This may be attributed to the circumstance that when a Ti atom enters into the Al lattice, it will produce lattice distortion and form compounds, consequently resulting in the decrease in diffraction peaks and changes of crystallite sizes. Since Al_3Ti has the lowest Gibbs standard free energy of formation among Al-Ti intermetallics, the nucleation of Al_3Ti is the most probable[41]. Although aluminium alloys have high sensitivity to oxygen, the diffraction peaks of aluminium oxide are not detected within the limitation of the XRD detection. This implies that the oxidation behaviour can be avoided in such protective atmosphere during LPBF preparation.

2.2 Variations of grain size and texture

Instantaneous energy from laser irradiation causes rapid melting and solidification in the molten pools. Greater undercooling (ΔT) at the solid-liquid interface front provides an energetically favourable condition and promotes nucleation and growth. Dependent on the ratio of thermal gradient (G) and growth rate (R), the mode of solidification and feature fineness can be determined[42]. The morphology of fine cell, as well as the anisotropy characteristic of the top surface can be observed in LPBF-processed AlSi10Mg sample, as shown in Fig. 6a. In the inverse pole figures (IPFs), different colours describe the distribution of different grains. The red, blue and green colours represent <001> , <111> and <101> grain orientations, respectively. Similar colours represent grains with the same orientation. When the addition proportion is 3wt% , grain sizes are inclined to be smaller and the morphology becomes almost finer (Fig. 6c). Fig. 6f presents a variation trend of grain sizes without and with 3wt% Ti addition. The minimum average grain sizes can be obtained to 0.969 μm, and the size range is within 2.5 μm. From the view of Fig. 6b and 6d, the grains in colour represent the sizes smaller than 1 μm. A relatively uniform grain distribution can be found in Fig.6d.

To further illustrate the influence of Ti addition on the microstructure, the grain boundary distribution and pole figure of LPBF-processed aluminium without and with 3wt% Ti

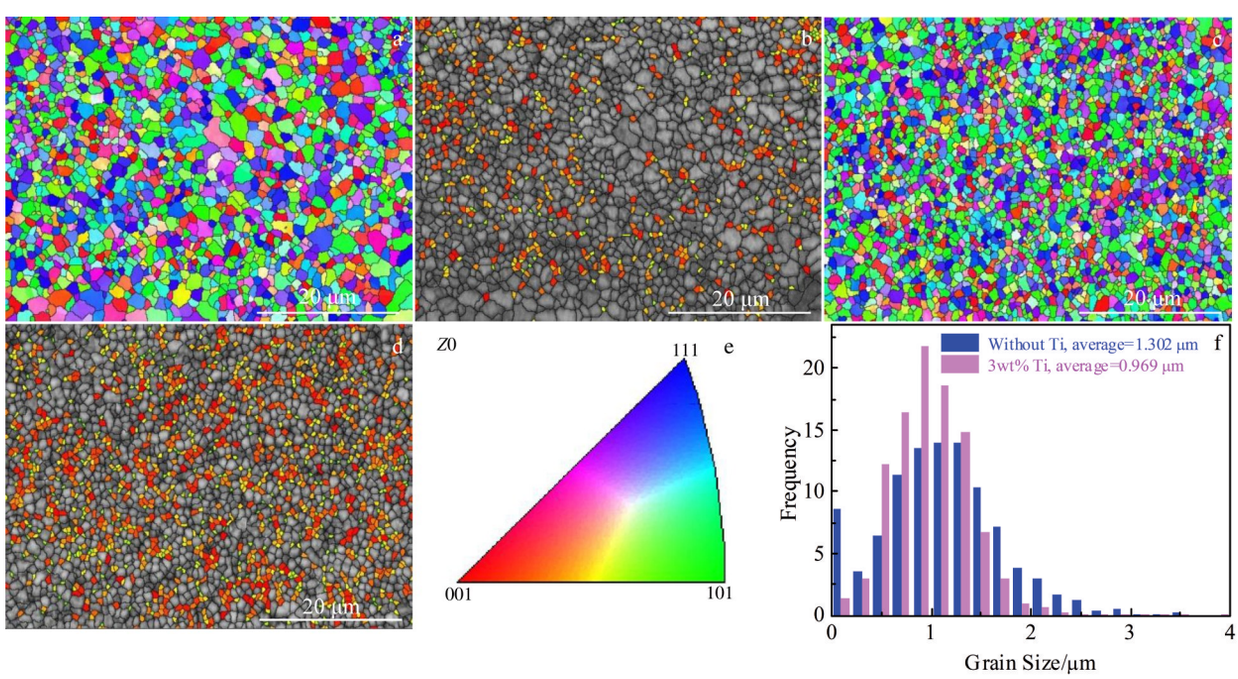

Fig.6 Grain morphology distributions without and with 3% Ti addition: (a, c) IPFs of the top surface; (b, d) grains in colour representing the sizes smaller than 1 μm with the step size of 0.13 μm; (e) grain misorientation; (f) distribution of grain sizes

addition are compared. Fig. 7a–7b display the grain boundary distribution of LPBF-processed samples without and with 3wt% Ti addition, respectively. The black lines represent high angle grain boundaries (HAGBs, >15°). The green lines represent low angle grain boundaries (LAGBs, <2°). After adding 3wt% Ti particles, the HAGBs are transformed to LAGBs partially, which will cause an increase in distortion energy. This verifies the formation of cell structures and the phenomenon of grain sizes refining, making an impact on the nano-hardness. During LPBF process, the laser scans the powders with long vectors in a zigzag fashion for each layer. Due to the moving heat source with a high scanning speed (v), the melt pool is elongated. A slightly strong <100> texture along the scanning direction can be observed in Fig. 7c. With introducing 3wt% Ti, the <100> texture is slightly enhanced; however, it still shows a weak texture intensity and random crystal orientation. It is well known that the solidification texture can be influenced by phase formation[43]. This can verify the occurrence of new phases, but with no preferred crystallographic texture. Further investigation should be conducted to reveal the underlying influencing mechanism of the Ti amount on the texture intensity of LPBF-processed aluminum alloys.

2.3 Precipitated phases and crystal structure

The grain sizes between 0.5–1 μm, and network morphologies with 3wt% Ti addition are depicted in Fig. 8a. As stated in Section 2.1 and Ref.[37–38], the network morphologies are identified to be an Al/Si eutectic phase, as well as the matrix phase of Al. With 3wt% Ti addition, there are a growing number of quadrilateral or anomalous phases precipitated at the grain boundary. To characterize chemical composition of these phases, which are labelled in colour, point scanning is adopted. Combined with EDS detection, the curves of element distribution are shown in Fig. 8b, and the mass or atomic percentage is also listed.

Combined with the results of Section 2.1 and Ref. [35], the precipitated phases are located both along the boundaries and inside the crystal grains. The diffraction spots of precipitated phases are pointed by a red circle in Fig.8c. According to high-resolution TEM (HRTEM) images and corresponding selective area electron diffraction (SAED) patterns, the crystal lattice parameters and identification can be determined. The lattice constants of α-Al is a=0.405 nm[35]. As shown in Fig.8d, in the exploration of Ti addition of 3wt%, Al_3Ti can be found with a tetragonal crystal structure and lattice parameters of a=b=0.3846 nm and c=0.8594 nm, which is almost consistent with the Pang ' s study[44]. Fan et al[45] verified that Al_3Ti particles have good atomic matching with α-Al and act as a highly effective nucleating agent. Combined with the element distribution analysis and XRD analysis, the precipitated phase is Al_3Ti. The crystal structures are shown in Fig. 8e, and the green balls and pink balls represent the Ti atom and Al atom,

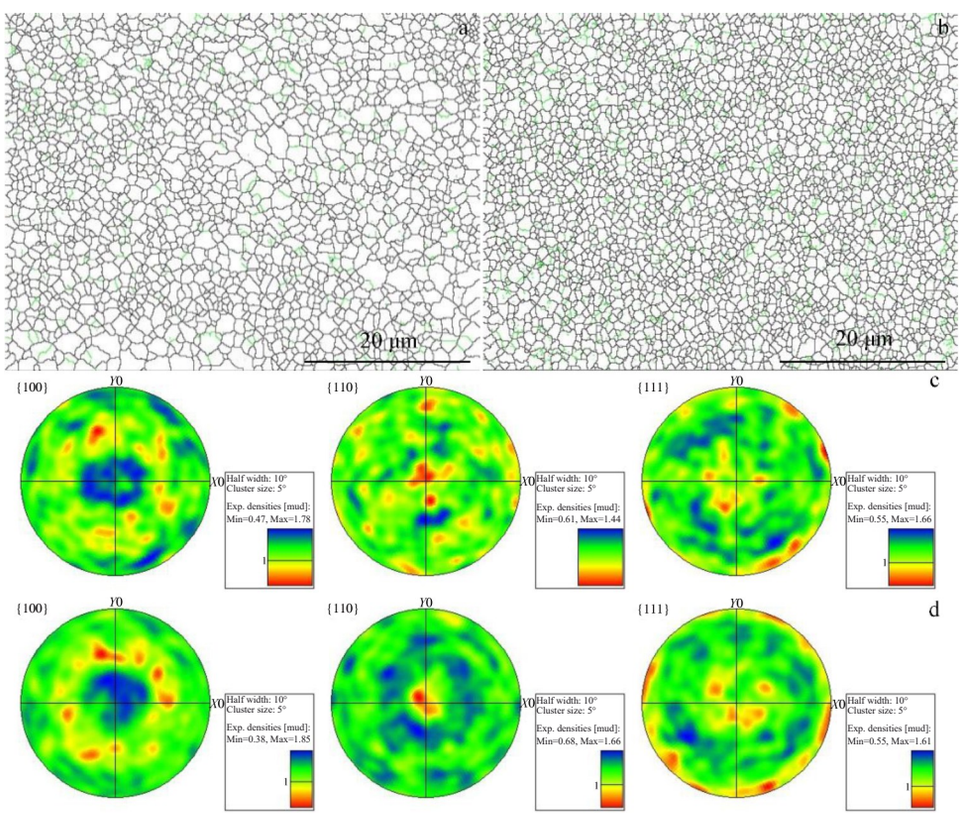

Fig.7 Comparison of LPBF-processed aluminium alloys without (a, c) or with (b, d) 3wt% Ti addition: (a–b) grain boundaries distribution and (c–d) pole figures

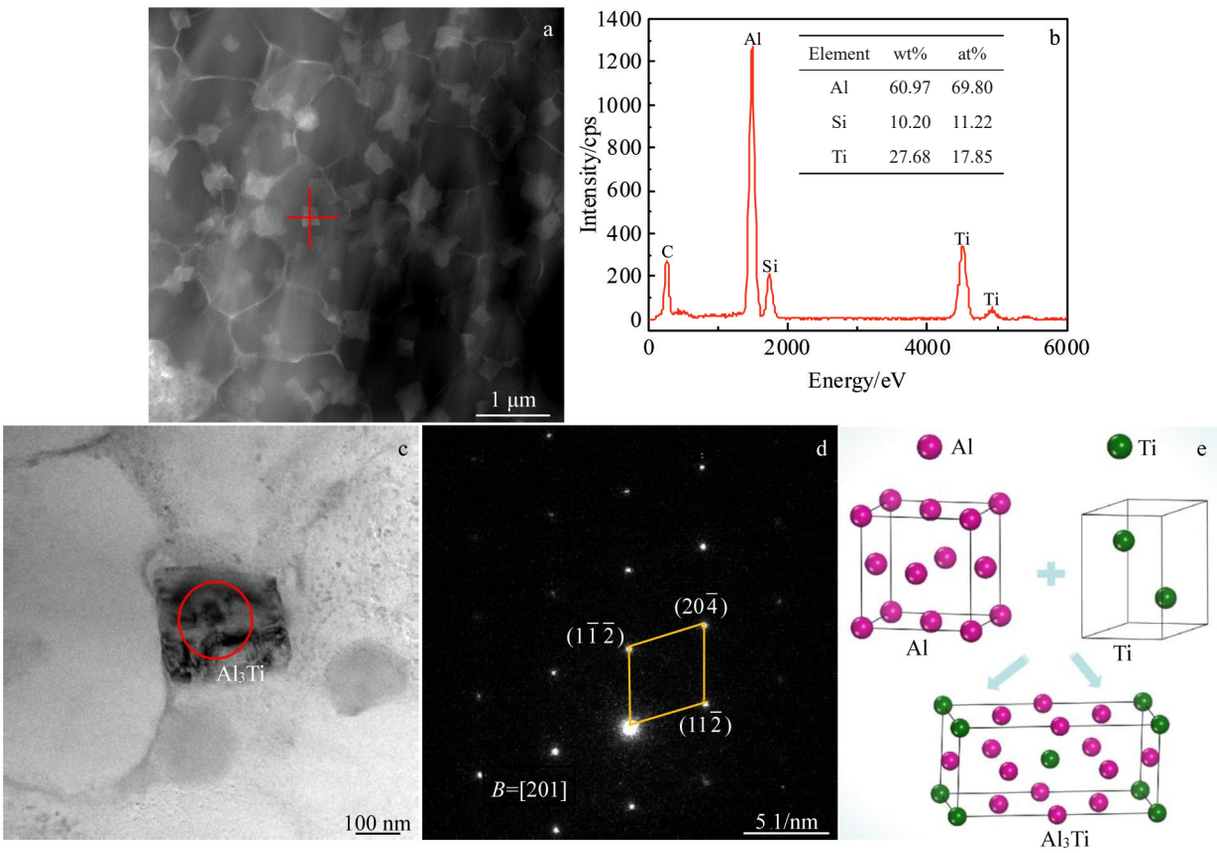

Fig.8 HRTEM image of network morphology and precipitated phases of as-built samples with 3wt% Ti addition (a) and corresponding EDS results of point labelled in Fig.8a (b); HRTEM image of precipitated phase upon the grain boundary with 3wt% Ti (c) and corresponding SAED pattern (d); schematic of crystal structures (e)

respectively. When the micro melt pool develops, the Ti atom enters into the Al lattice, forming Al-Ti compounds. According to the evaluation by first principle calculations, the cohesive energy (E_{coh}) is −6.639, −5.707 and −4.193 eV for Al_3Ti, AlTi and $AlTi_3$, respectively[46]. In consequence, Al_3Ti is the preferential formation phase in Al-Ti compounds. Combined with the results of reduced grain sizes, the Al_3Ti particles can not only promote the nucleation of α-Al, but also accelerate the morphology transition to equiaxed grains, refining the grains.

2.4 Nano-hardness and Young's modulus

As stated above, the changes in grain sizes and distortion energy have impact on nano-hardness and Young's modulus. In this study, the NanoBlitz 3D release method implemented in the iNano instrument was used to characterize the LPBF-processed samples without and with 3wt% Ti addition. The nano-hardness (H) can be defined as follows[47]:

$$H = \frac{P}{A} \tag{2}$$

where P is the maximum load and A is the projected area of the indentation. The Young's modulus (E_r) can be expressed by the following equation:

$$E_r = \frac{\sqrt{\pi}}{2\beta}\frac{S}{\sqrt{A}} \tag{3}$$

where β is constant (1.034) and S is the contact stiffness. The corresponding highly resolved maps of nano-hardness and Young's modulus are created, as shown in Fig. 9a–9d. The x-axis determines the position of the nano-indentation point. After adding 3wt% Ti powders, the average nano-hardness values of microstructure increase dramatically from 1.88 GPa to 2.36 GPa. Notably, the achieved value is more than two times larger than that of as-cast AlSi10Mg alloy (about 0.97 GPa)[32]. Meanwhile, the average Young's modulus values increase to 92.72 GPa. As can be seen from closer observation in Fig. 9d, some values are larger than 110 GPa, which are in the reported range of Al-Ti intermetallic compounds[48].

According to the Hall-Petch relationship, the yield strength is inversely proportional to the grain sizes. Grain refinement can be induced by the effect of heterogeneous nucleation. However, the precipitated phases belong to brittle phases within a high stiffness, which may have a deteriorative effect on strength-ductility trade-off. Thereby, the influence of intermetallic compounds amount on the final mechanical properties of LPBF-processed samples with different Ti proportions needs to be further explored.

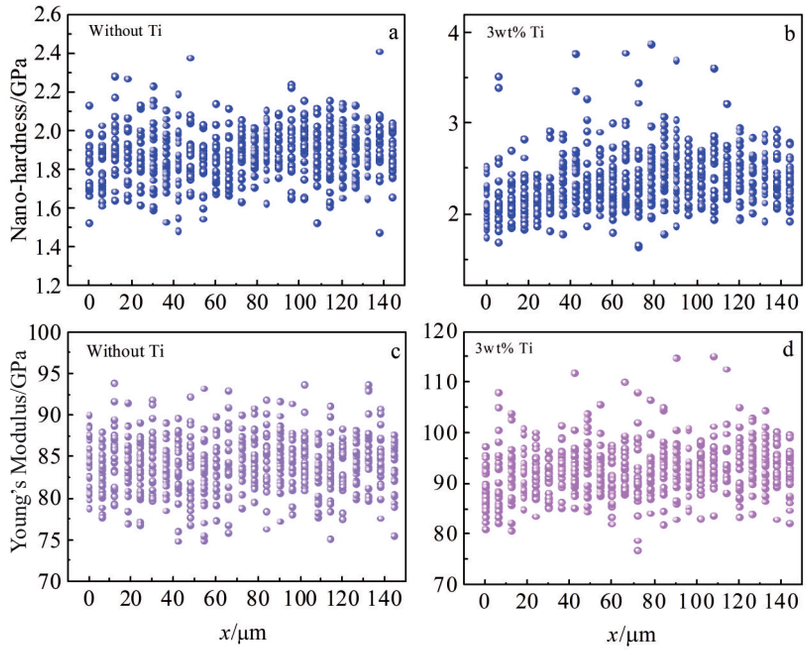

Fig.9 Mechanical properties of LPBF-processed aluminum alloys without and with 3wt% Ti addition: (a–b) nano-hardness and (c–d) Young's modulus

3 Conclusions

1) The influence of 3wt% Ti addition on the microstructure characteristics and phase identification of LPBF-processed Al-based alloys is investigated. Depending on factors of temperature gradient and solidification rate, the microstructure displays a fine cell-like substructure with anisotropy characteristics.

2) When 3wt% Ti is added, precipitated phases are distributed along the grain boundary or inside the grains. The heterogeneous nucleation effect of substantial precipitated phases promotes the grain refinement and reduces the grain sizes. The precipitated phase has tetragonal Al_3Ti crystal structure, but operates little effect on texture intensity and crystal orientation.

3) The transformation of HAGBs into LAGBs promotes the increase in distortion energy. The average nano-hardness and Young's modulus of the LPBF-processed Al-based sample with 3wt% Ti addition can increase to approximately 2.36 and 92.72 GPa, respectively. The influence of increasing Ti amount on the microstructure evolution, formation of intermetallic compounds as well as the mechanical properties needs to be further investigated.

References

1 Guan J R, Wang Q P. *Materials*[J], 2023, 16(7): 2757

2 Sing S L, Yeong W Y. *Virtual and Physical Prototyping*[J], 2020, 15: 359

3 Zhang J L, Song B, Wei Q S *et al. Journal of Materials Science & Technology*[J], 2019, 35: 270

4 Aboulkhair N T, Everitt N M, Ashcroft I *et al. Additive Manufacturing*[J], 2014,1–4: 77

5 Olakanmi E O, Cochrane R F, Dalgarno K W *et al. Progress in Materials Science*[J], 2015, 74: 401

6 Cui X M, Liang S B, Zhao X P *et al. Rare Metal Materials and Engineering*[J], 2023, 52(5): 1603

7 Wei H L, Elmer J W, Debroy T. *Acta Materialia*[J], 2016, 115: 123

8 Chowdhury S, Yadaiah N, Prakash C *et al. Journal of Materials Research and Technology*[J], 2022, 20: 2109

9 Mao B Y, Liu Y, Ye J W *et al. Rare Metal Materials and Engineering*[J], 2023, 52(3): 860

10 Zheng M, Wei L, Chen J *et al. Journal of Materials Research and Technology*[J], 2021, 11: 392

11 Volpato G M, Tetzlaff U, Fredel M C. *Additive Manufacturing*[J], 2022, 55: 102871

12 Tian Z H, Zhang C Q, Wang D Y *et al. Applied Science*[J], 2020, 10(1): 81

13 Ma Z B, Zhang K F, Ren Z H *et al. Journal of Alloys and Compounds*[J], 2020, 828: 154350

14 Mao Z F, Zhang D, Wei P T *et al. Materials*[J], 2017, 10: 333

15 Tang X P, Chen X H, Sun F J *et al. Journal of Alloys and Compounds*[J], 2022, 924: 166627

16 Liu Y G, Zhang J Q, Tan Q Y *et al. Optics and Laser Technology*[J], 2021, 134: 106649

17 Luo X, Li D D, Yang C *et al. Additive Manufacturing*[J], 2022, 51: 102640

18 He B B, Wu W H, Zhang L *et al. Vacuum*[J], 2018, 150: 79

19 Miller W S, Zhuang L, Bottema J *et al. Materials Science and Engineering A*[J], 2000, 280: 37

20 Aversa A, Marchese G, Sabbori A *et al. Materials*[J], 2019, 12(7): 1007
21 Kang N, Coddet P, Liao H L *et al. Applied Surface Science*[J], 2016, 378: 142
22 Read N, Wang W, Essa K *et al. Materials and Design*[J], 2015, 65: 417
23 Li W, Li S, Liu J *et al. Materials Science and Engineering A*[J], 2016, 663: 116
24 Tradowsky U, White J, Ward R M *et al. Materials and Design*[J], 2016, 105: 212
25 Trevisan F, Calignano F, Lorusso M *et al. Materials*[J], 2017, 10: 76
26 Brandl E, Heckenberger U, Holzinger V *et al. Materials and Design*[J], 2012, 34: 159
27 Dadbakhsh S, Mertens R, Hao L *et al. Advanced Engineering Materials*[J], 2019, 21: 3
28 Wang H Q, Gu D. *Journal of Composite Materials*[J], 2015, 49(13): 1639
29 Yuan P, Gu D. *Journal of Physics D-Applied Physics*[J], 2015, 48: 035303
30 Zhao X, Song B, Fan W *et al. Journal of Alloys and Compounds*[J], 2016, 665: 271
31 Li X P, Ji G, Chen Z *et al. Acta Materialia*[J], 2017, 129: 183
32 Zhao X, Gu D, Ma C L *et al. Vacuum*[J], 2019, 160: 189
33 Martin J H, Yahata B D, Hundley J M *et al. Nature*[J], 2017, 549: 365
34 Zhao H L, White D R, Debroy T. *Metallurgical Reviews*[J], 1999, 44: 238
35 Zhang J L, Gao J B, Song B *et al. Additive Manufacturing*[J], 2020, 38: 101829
36 Wu J, Wang X Q, Wang W *et al. Acta Materialia*[J], 2016, 117: 311
37 Kim D K, Woo W, Hwang J H *et al. Journal of Alloys and Compounds*[J], 2016, 686: 281
38 Thijs L, Kempen K, Kruth J P *et al. Acta Materialia*[J], 2013, 61: 1809
39 Kuryntsen S. *Materials*[J], 2022, 15: 122
40 Han Q, Setchi R, Evans S L. *International Journal of Advanced Manufacturing Technology*[J], 2017, 88: 1429
41 Foadian F, Soltanieh M, Adeli M *et al. Metallurgical and Materials Transaction A*[J], 2014, 45(4): 1823
42 Wang Q, Zhang S, Zhang C H *et al. Vacuum*[J], 2017, 141: 38
43 Suwas S, Ray R K. *Crystallographic Texture of Materials*[M]. New York: Springer, 2014
44 Pang X Z, Chen X X, Yang J B *et al. Journal of Physics and Chemistry of Solids*[J], 2019, 131: 243
45 Fan Z, Wang Y, Zhang Y *et al. Acta Materialia*[J], 2015, 84: 292
46 Jian X, Huang Z F, Xing J D *et al. Materials Chemistry and Physics*[J], 2019, 221: 311
47 Oliver W C, Pharr G M. *MRS Bulletin*[J], 2010, 35: 897
48 Lipsitt H A. *Materials Research Society Symposium Proceedings*[C]. Pennsylvania: Materials Research Society, 1985: 39

LPBF成型加Ti铝基合金的组织特性及其对纳米硬度的影响

王秋平，关杰仁
(江苏科技大学 海洋装备研究院，江苏 镇江 212003)

摘　要：论述了在激光粉末床熔融（LPBF）成型Al基合金中添加Ti的影响。采用扫描电镜、电子背散射衍射、X射线衍射、透射电镜和纳米压痕测试等方法，研究了Ti含量为3%（质量分数，下同）和不含Ti的LPBF制备样品的显微组织特征、相分布和纳米硬度。结果表明，该方法可获得较细的晶粒组织和较小的平均晶粒尺寸。由于Al_3Ti析出相的非均相形核，晶粒尺寸范围减小到2.5 μm以内。随着小角度晶界的增大，晶格畸变能增大，平均纳米硬度和杨氏模量分别提高到2.36和92.72 GPa。添加3% Ti后，LPBF处理的Al基合金<100>织构略有增强，但仍有一个随机的晶体取向。获得了α-Al向Al_3Ti的相变。

关键词：激光粉床熔融；组织；析出相；纳米硬度；晶粒尺寸

作者简介：王秋平，女，1989年生，博士，讲师，江苏科技大学海洋装备研究院，江苏 镇江 212003，E-mail：a21096@163.com